Electronic Supplementary Material (ESI) for Materials Horizons.
This journal is © The Royal Society of Chemistry 2023

Supplementary Information

High entropy alloying strategy for accomplishing quintuple nanoparticles grafted carbon towards exceptional high-performance overall seawater splitting

Gokul Raj [a,#], Ravi Nandan [a,#], Kanhai Kumar [a], Demudu Babu Gorle [a], Ambresh B Mallya [b], Sameh M. Osman [c], Jongbeom Na [d,e], Yusuke Yamauchi [c,e,f] and Karuna Kar Nanda [a,g,]**

[a] *Materials Research Centre, Indian Institute of Science, Bangalore-560012, Karnataka, India.*

[b] *Micro Nano Characterization Facility, Centre for Nano Science and Engineering. Indian Institute of Science, Bangalore-560012, India.*

[c] *Chemistry Department, College of Science, King Saud University, Riyadh 11451, Saudi Arabia.*

[d] *Materials Architecturing Research Center, Korea Institute of Science and Technology (KIST), 5 Hwarang-ro 14-gil, Seongbuk-gu, Seoul 02792, Republic of Korea.*

[e] *Australian Institute for Bioengineering and Nanotechnology (AIBN), The University of Queensland, Brisbane, QLD 4072, Australia.*

[f] *Department of Materials Process Engineering, Graduate School of Engineering, Nagoya University, Nagoya 464–8603, Japan.*

[g] *Institute of Physics (IOP), Bhubaneshwar-751005, India.*

[*] *E-mails: nanda@iisc.ac.in; jongbeom@kist.re.kr*

[#] *The authors have equally contributed to this work.*

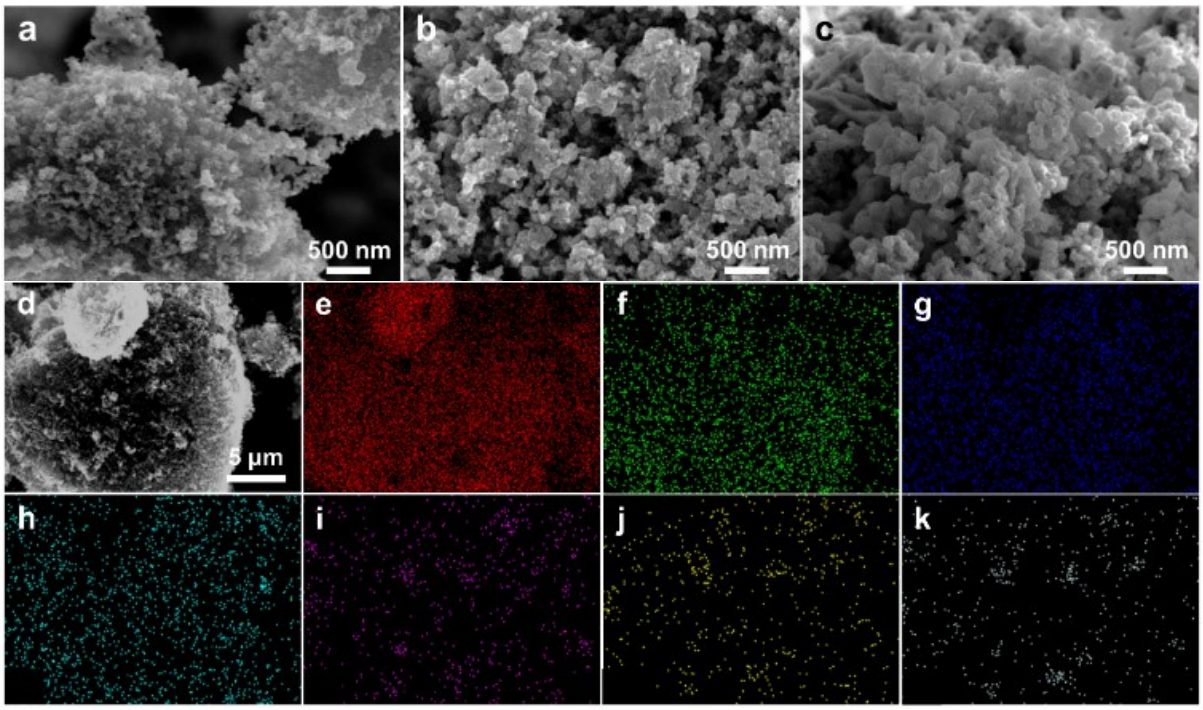

Fig. S1. SEM images of (a) HEACB 500, (b) HEACB 750, and (c) HEACB 1000, (d) Selected SEM image of HEACB 1000 for elemental portioning along with (e) C, (f) O, (g) Cr, (h) Mn, (i) Fe, (j) Co, and (k) Ni, elemental maps respectively.

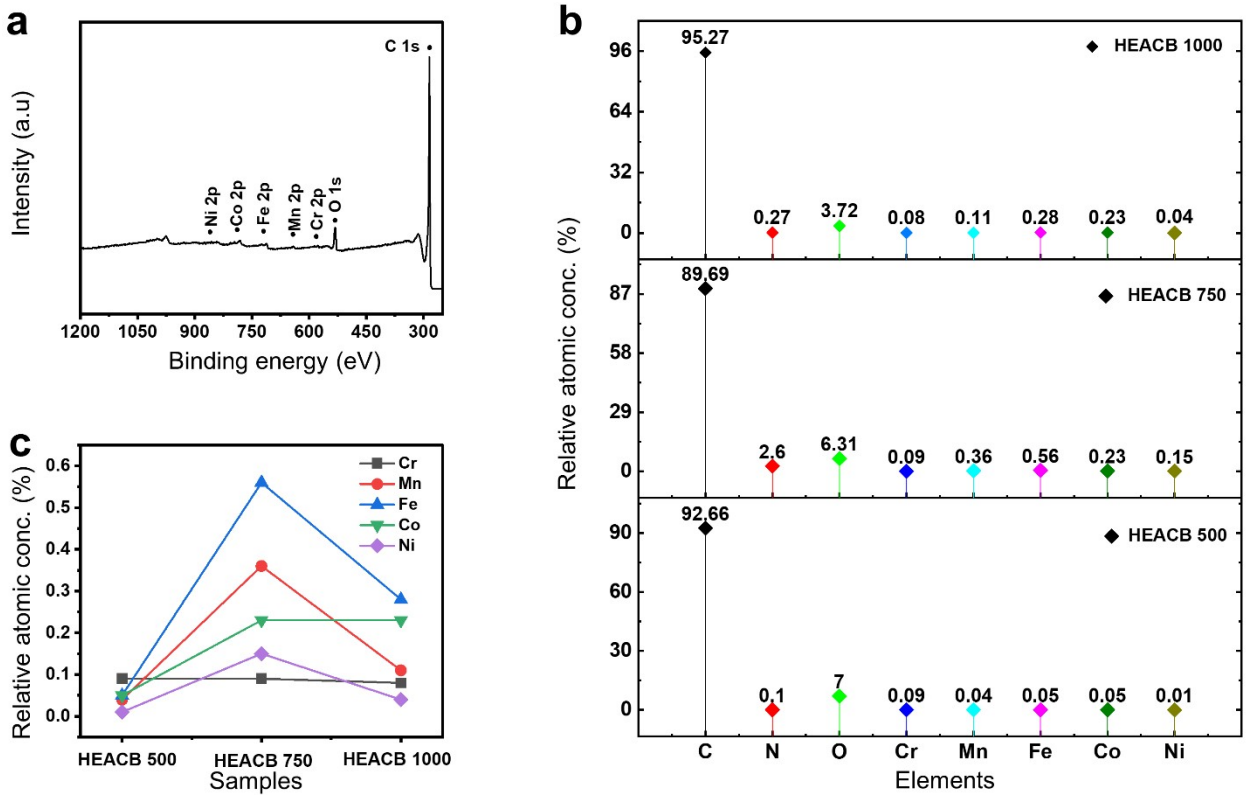

Fig. S2. (a) Wide XPS spectrum of HEACB 1000, (b) Elemental ratios extracted from XPS data for HEACB 1000, HEACB 750, and HEACB 500. The overall total atomic concentrations of the metals (Cr, Mn, Fe, Co, and Ni) are 0.24% for HEACB 500, 1.39% for HEACB 750, and 0.74% for HEACB 1000. (c) Variation of relative atomic percentages of Cr, Mn, Fe, Co, and Ni only, across HEACBs, deduced from Fig. S2b.

Text associated with Fig. S2

Fig. S2b shows the compositional details of HEACBs, deduced from XPS study. The total metallic content for HEACB500, HEACB750, and HEACB1000 are 0.24, 1.39, and 0.74 % respectively, indicating the effect of synthesis temperature on total metallic content in composites. Fig. S2c shows the variation of individual metallic concentrations in HEACBs. The internal metal composition (Fe:Co:Ni:Mn:Cr) of HEA, as deduced from XPS, in HEACBs composites is found to be 21:21:4:37:17 (for HEACB500), 40:16:11:7:26 (for HEACB 750) and 38:31:5:11:15 (for HEACB1000).

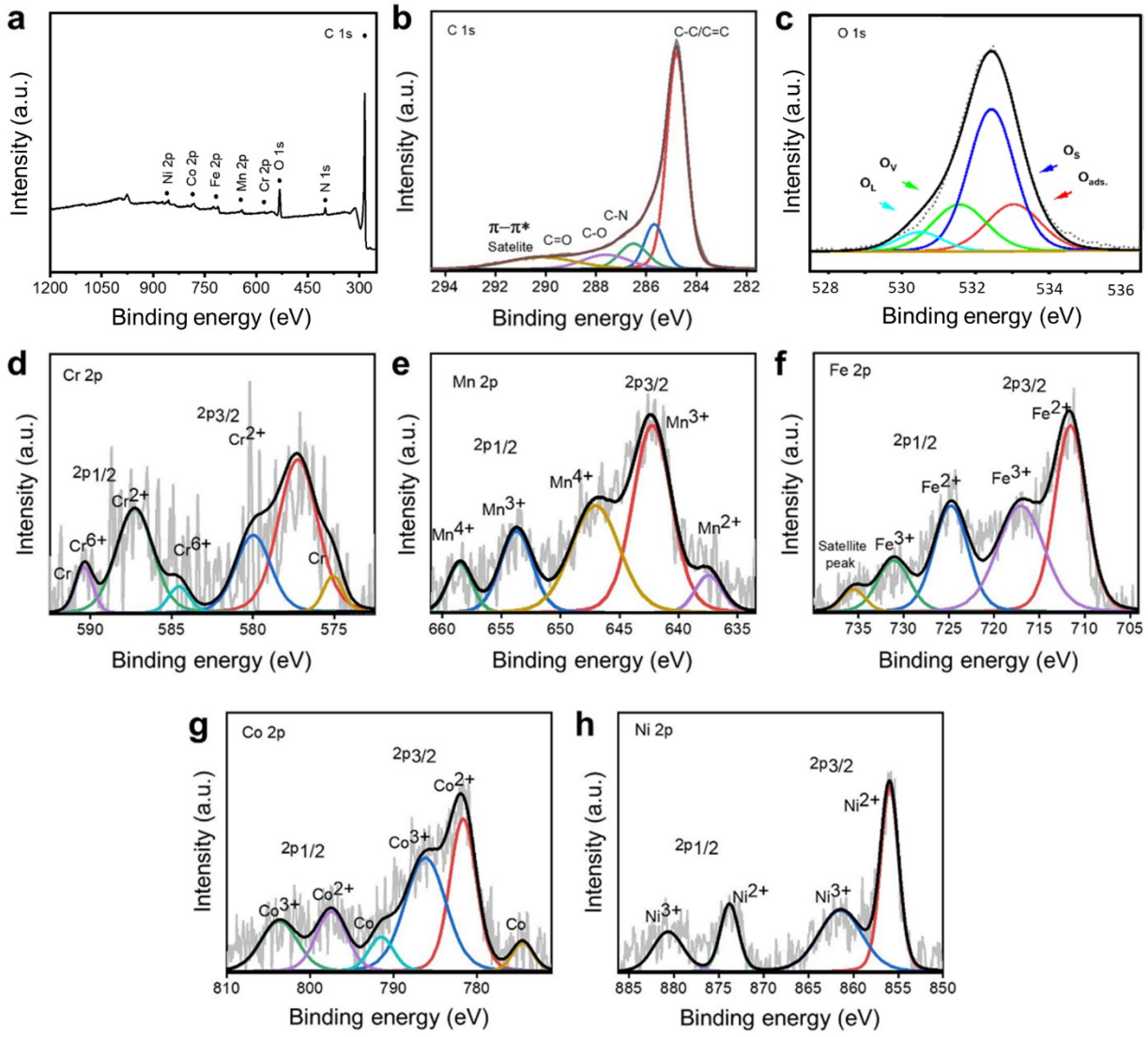

Fig. S3. XPS survey spectrum of HEACB 750 (a). HRXPS spectra of (b) C 1*s*, (c) O 1*s*, (d) Cr 2*p*, (e) Mn 2*p*, (f) Fe 2*p*, (g) Co 2*p*, and (h) Ni 2*p*.

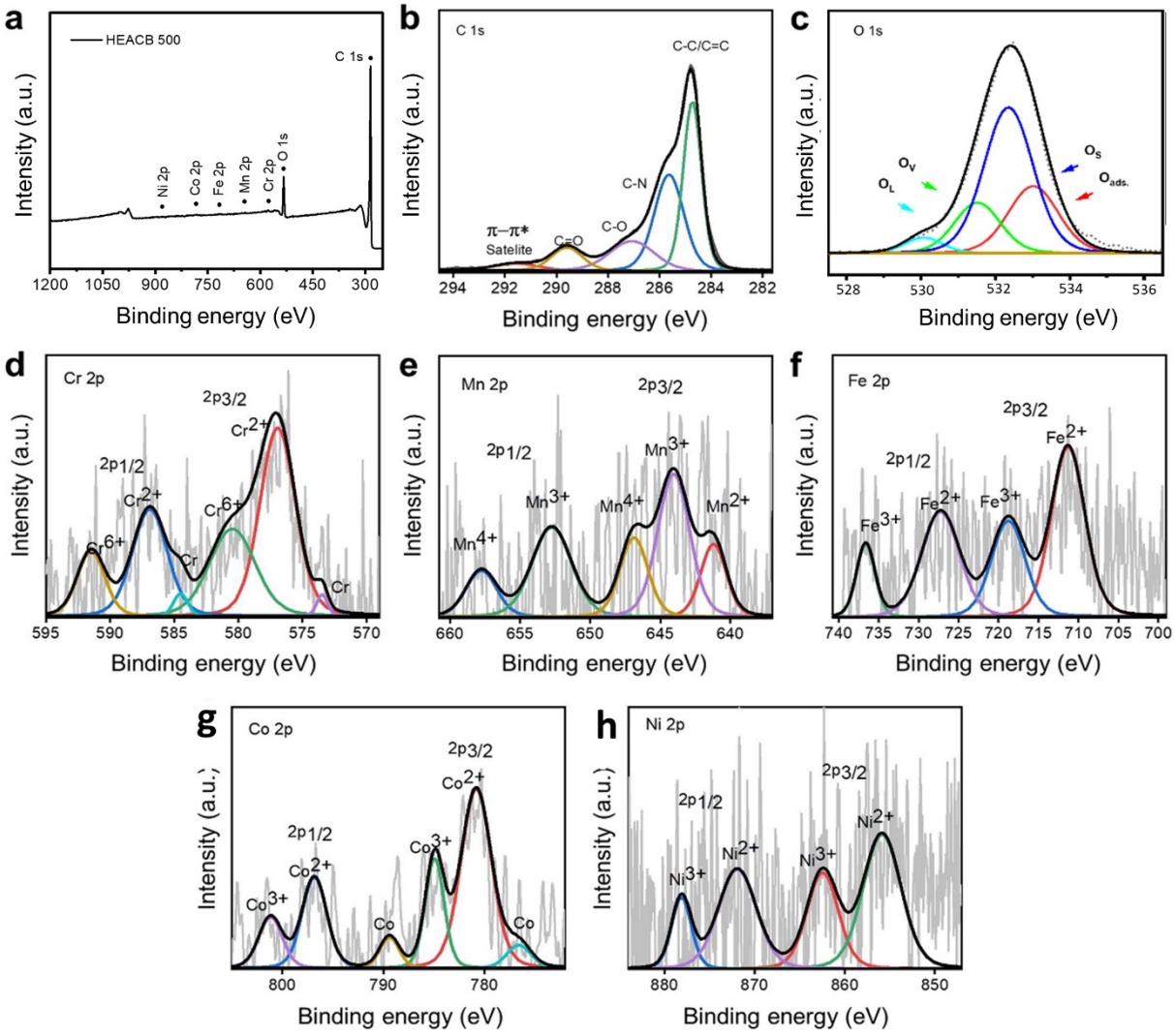

Fig. S4. XPS survey spectrum of HEACB 500 (a). HRXPS spectra of (b) C 1*s*, (c) O 1*s*, (d) Cr 2*p*, (e) Mn 2*p*, (f) Fe 2*p*, (g) Co 2*p*, and (h) Ni 2*p*.

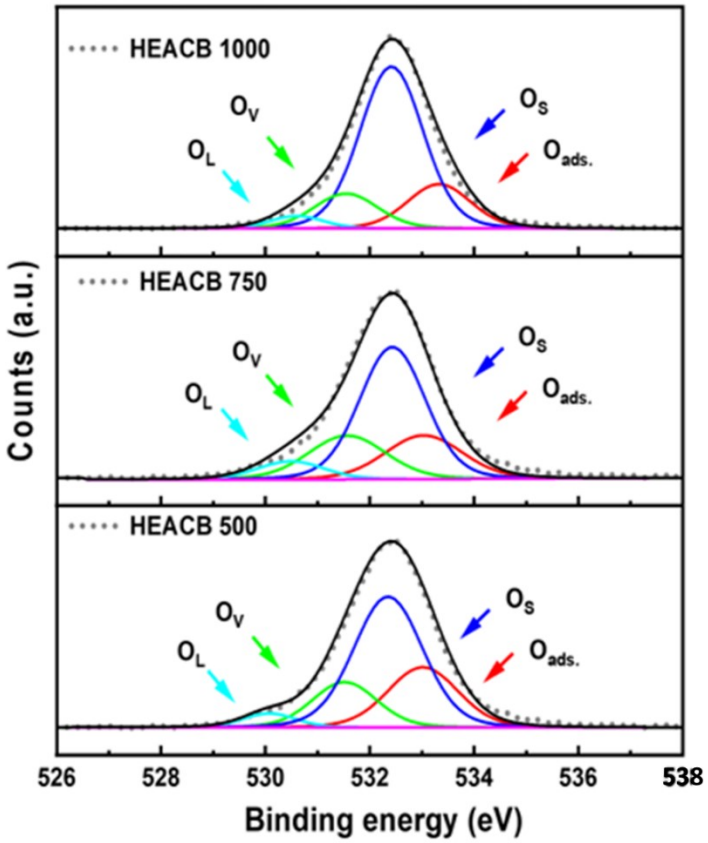

Fig. S5. High-resolution XPS spectra of O1s for HEACBs samples.

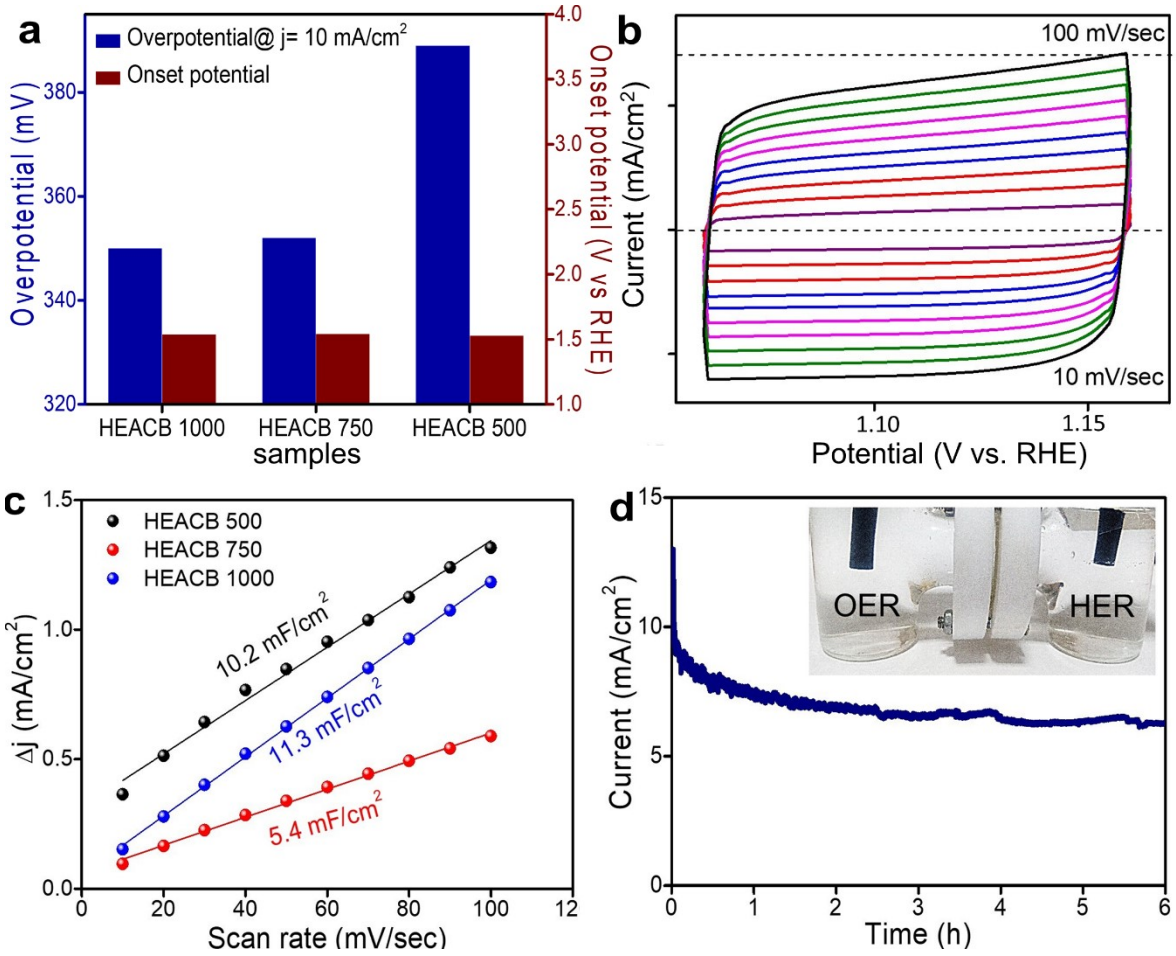

Fig. S6. (a) Comparison of onset and overpotential of all samples in the OER polarization region in 1M KOH, (b) CVs curves on HEACB 1000 in the non-faradaic region in 1M KOH medium. (c) Charged double layer capacitance comparison for HEACB 1000, HEACB 750, and HEACB 500, and (d) chronoamperometry test for HEACB 1000 in 1M KOH at room temperature in the OER polarization potential (inset: H cell setup for bulk water electrolysis).

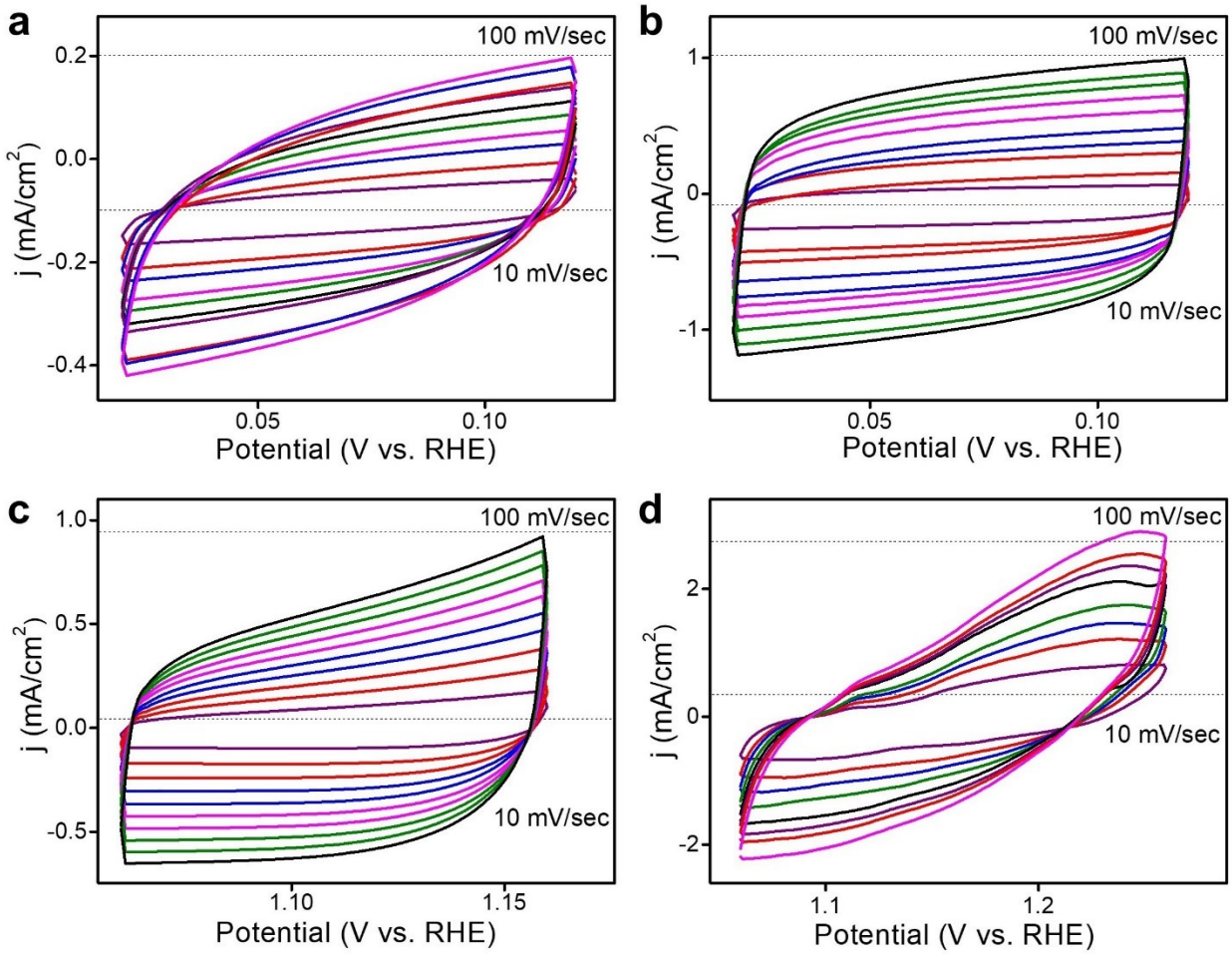

Fig. S7. CV curves at (a, c) HEACB 750 and (b, d) HEACB 500 in acidic and basic electrolytic solutions respectively.

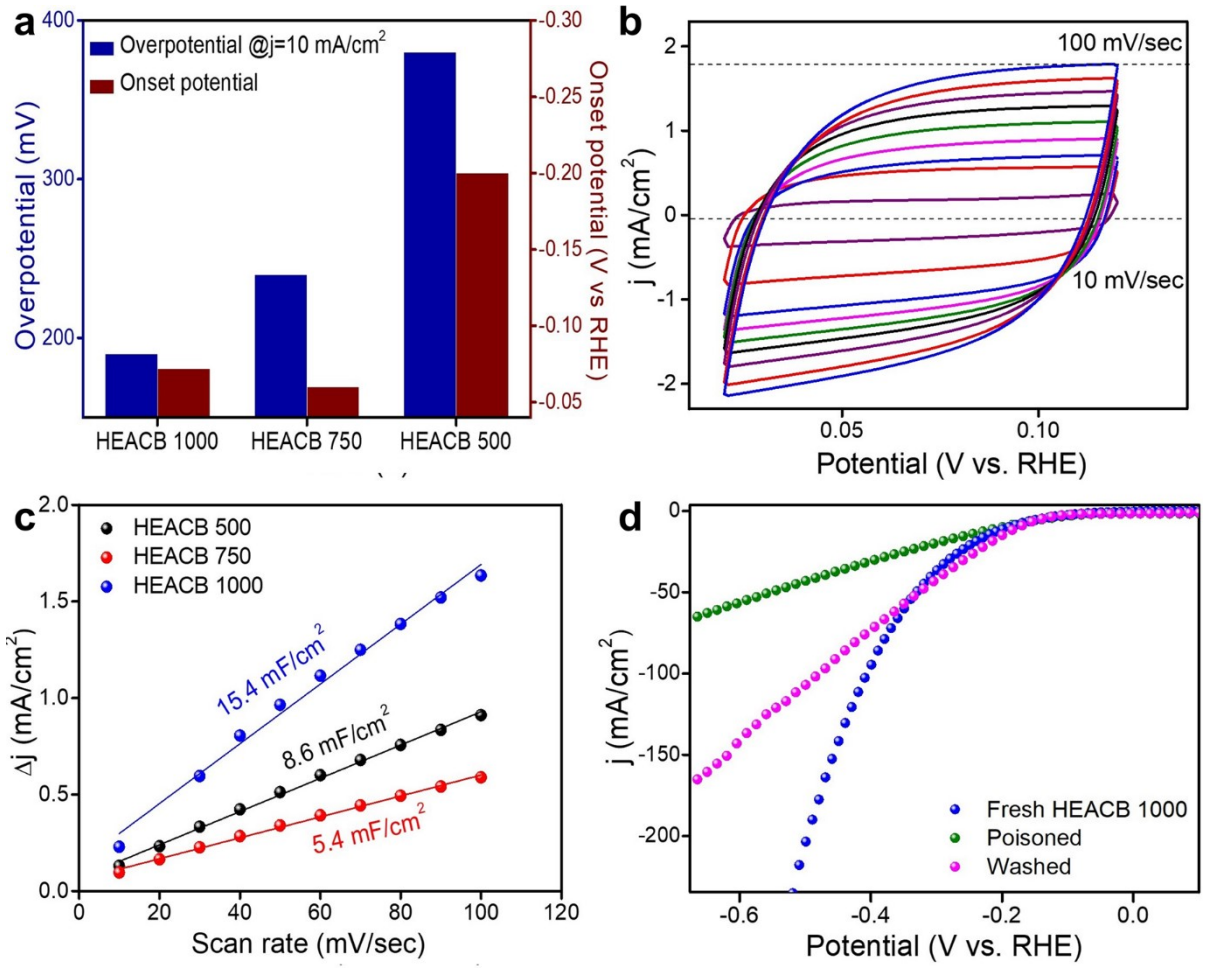

Fig. S8. (a) Comparison of onset and overpotential of all samples in the HER polarization region in 0.5M H_2SO_4, (b**)** CV at HEACB 1000 in the non-faradaic region in 0.5 M H_2SO_4 medium. (c) Charged double layer capacitance comparison for HEACB 1000, 750, and 500 in 0.5 M H_2SO_4, and (d) LSV of the fresh, poisoned, and washed HEACB 1000 in the HER polarization region.

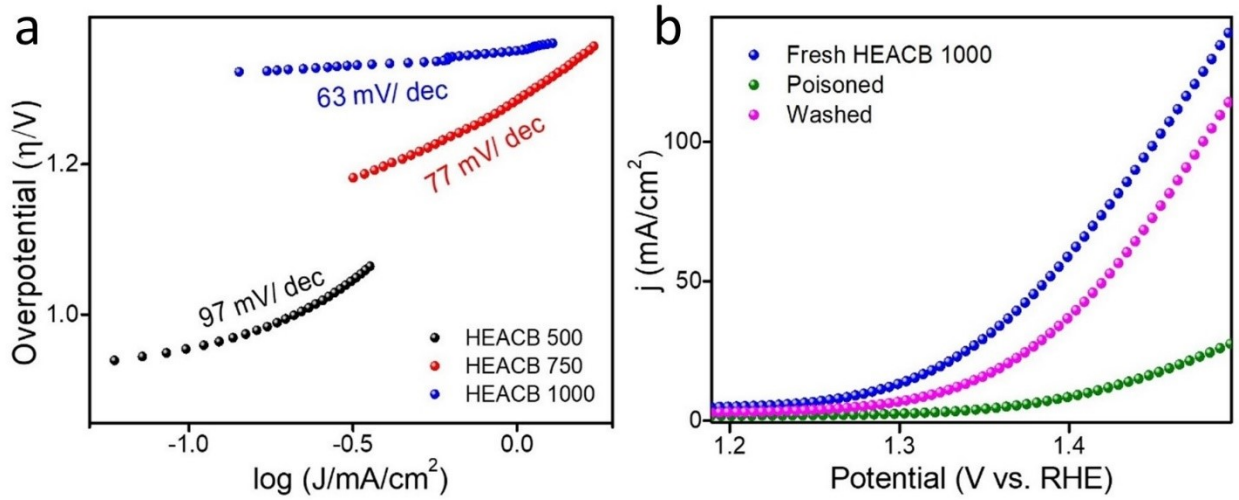

Fig. S9. (a) Tafel plots for the respective polarization curves in the CER polarization region in 1M H_2SO_4 and 4M NaCl, (b) LSV of the fresh, poisoned, and washed HEACB 1000 in the CER polarization region in 0.5M H_2SO_4 and 4M NaCl.

Post studied samples characterization

Along with performance, stability is crucial for the practical implementation of a catalyst on a real-time system. To improve our catalyst's stability and understand its deteriorative factors, we conducted a detailed chemical and structural analysis of our best-performing sample, HEACB 1000. This analysis aims to evaluate whether the catalyst can withstand the harsh reaction conditions of seawater splitting and to gain insights into any chemical changes at an atomic scale. For the post-characterization studies, we used a HEACB 1000-modified electrode on a three-electrode configuration setup where potentials were induced with respect to the Ag/AgCl reference electrode. The catalyst was then tested to sustain a current of approximately 10 mA/cm^2 under the HER, OER, and CER polarization regions. Each reaction was executed continuously for approximately 5 hours to assess the catalyst's ability to withstand the harsh conditions of overall seawater splitting. After completion of the reactions, the post-HEACB 1000 samples carefully extracted from the electrode surface to avoid contamination, dried thoroughly and kept under vacuum, and subjected to detailed chemical and structural characterization.

In the first phase of analysis, we performed X-ray diffraction (XRD) studies on the post-HEACB 1000 sample. Our primary focus is to determine whether the catalyst crystal structure remains intact or undergoes deformation and phase segregation due to oxidative degradation and leaching in the harsh oxidative potentials of OER and CER reactions. Chlorine water, which is highly corrosive, can accelerate the degradation process. **Fig. S10** shows the XRD pattern of the post-HEACB 1000 sample. From the XRD data, it is confirmed that the prominent peaks at 44.1°, 51.4°, and 75.5° correspond to the major plane reflection from the face-centered cubic (FCC) high entropy alloy system, like what we observe in the fresh sample of HEACB 1000. Any other prominent peaks corresponding to possible oxide formation and phase segregations are not observed, indicating the material's chemical and structural integrity remains intact even after exposure to a simulated seawater environment with considerable total water splitting performance. Therefore, XRD analysis indicates that the material shows decent stability with the least indication of leaching and chemical oxidation-induced phase segregations. This considerable stability can be attributed to the protective and conductive carbon coating provided by the supporting matrix CB, which prevents particle agglomeration, leaching, and possible phase segregation, along with improved electrical conductivity and mass transport rates. This finding underscores the importance of decorating our quintuple high entropy systems on conductive substructures.

To obtain visual images of the post-studied sample and evaluate morphological and chemical conditions, SEM observation was performed along with EDS mapping to obtain a quantitative estimation of the elements after the reactions. **Fig. S11** shows the representative SEM images of HEACB 1000 post-studied sample and the corresponding elemental maps. We did not observe any noticeable agglomeration which can be seen in the SEM images, even though HEACB1000 was exposed for the long time in the harsh chloride ion-containing seawater electrolytes. This clearly underlines the fact that the uniform distribution of alloys largely remains intact even after the long-term continuous operation of about 15 hours, indicating its strong chemical stability. It is interesting to note that the source of extra elements like K^+ and Cl^- are from the 4M chloride-containing electrolyte, and the S and F come directly from the Nafion binder used for preparing the modified electrode surfaces. To obtain more high-resolved images of the post-sample, the sample was subjected again to detailed TEM elemental analysis (**Fig. S12 and Table S9**). The HRTEM images, and the elemental maps are also in line with the SEM analysis. All five elements

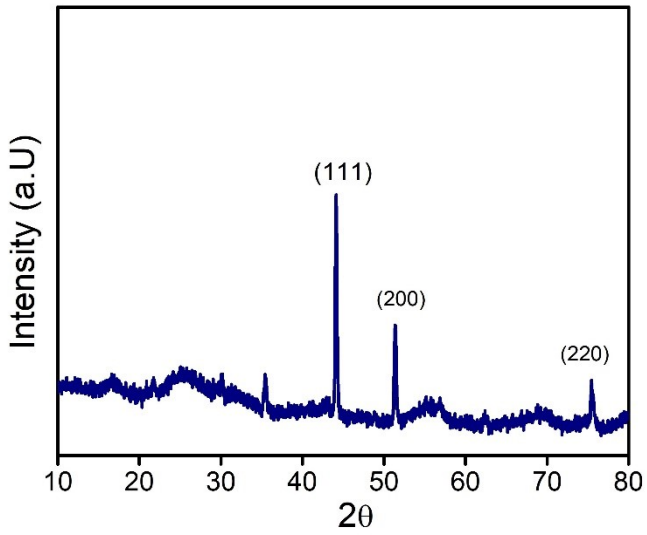

of the alloy are found to be still uniformly distributed on the observed particles (**Table S9**).

Fig. S10. XRD pattern of post-studied HEACB 1000 after subjecting it to the HER, OER and CER polarization regions consecutively in 0.5 H_2SO_4, 1 M KOH and 1M KOH-4M NaCl respectively.

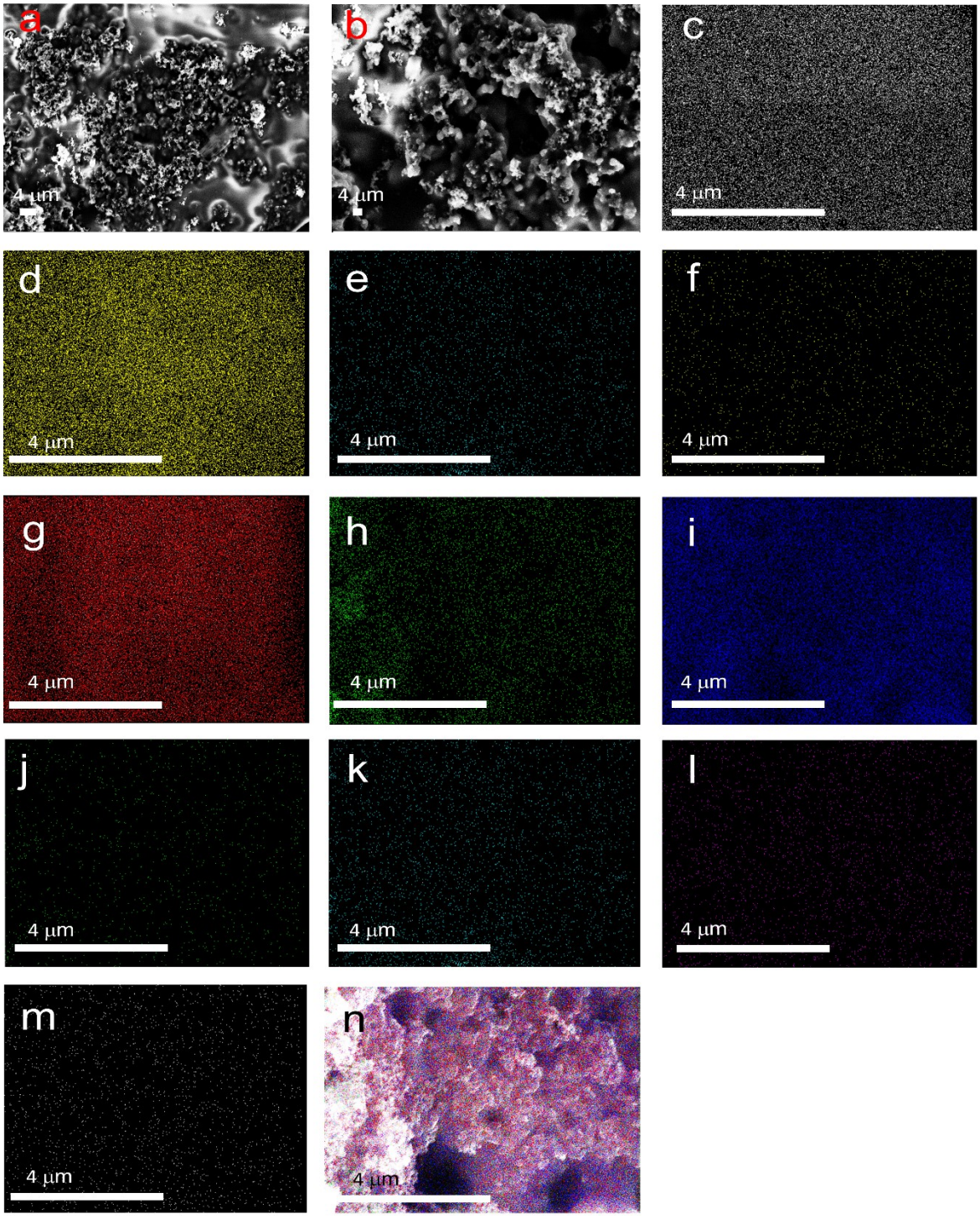

Fig. S11. (a-b) SEM images of post-studied HEACB 1000, (c-n) elemental mapping of the sample in the order Cl, S, K, Co, C, O, F, Ni, Fe, Cr, Mn and combined elemental map respectively.

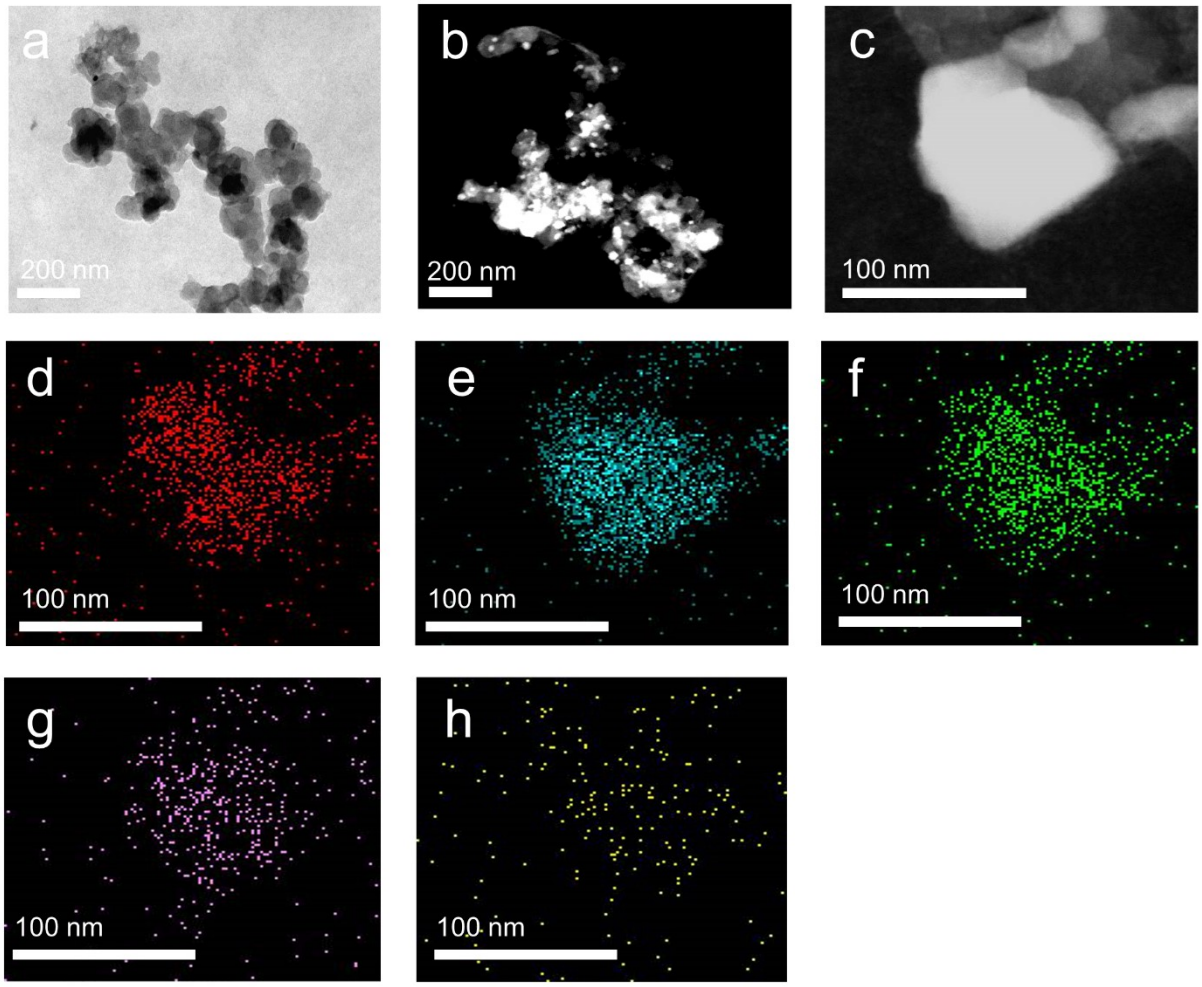

Fig. S12. Post-study HEACB 1000 (a) bright field and (b-c) dark field TEM images, (d-h) elemental mapping (Cr, Fe, Mn, Co, and Ni respectively) over the representative TEM image (c).

Kinetic parameter calculation

The Faradic efficiency, Exchange current density, and Turnover frequency were determined through standard experimental procedures and mathematical formulations reported in the literature.[2,3] The calculations were done using equations included in the appendix of the main text.

Calculation of Faradaic efficiency of OER reaction

F.E = (0.009 L × 4 × 96485 C) / (24.5 L × 162.4 C)

= 87.3 %

Calculation of Faradaic efficiency of HER reaction

F.E = (0.0072 L × 2 × 96485 C) / (24.5 L × 62 C)

= 91.5 %

Calculation of exchange current density (J_0)

Calculation for OER

J_0 = 8.3314 × 298 / (4 × 96485 × 12 × 0.07)

=7.5 mA/cm^2

Calculation for HER

J_0 = 8.3314 × 298 / (2 × 96485 × 13 × 0.07)

=14 mA/cm^2

Calculation for CER

J_0 = 8.3314 × 298 / (2 × 96485 × 12 × 0.07)

=15.2 mA/cm^2

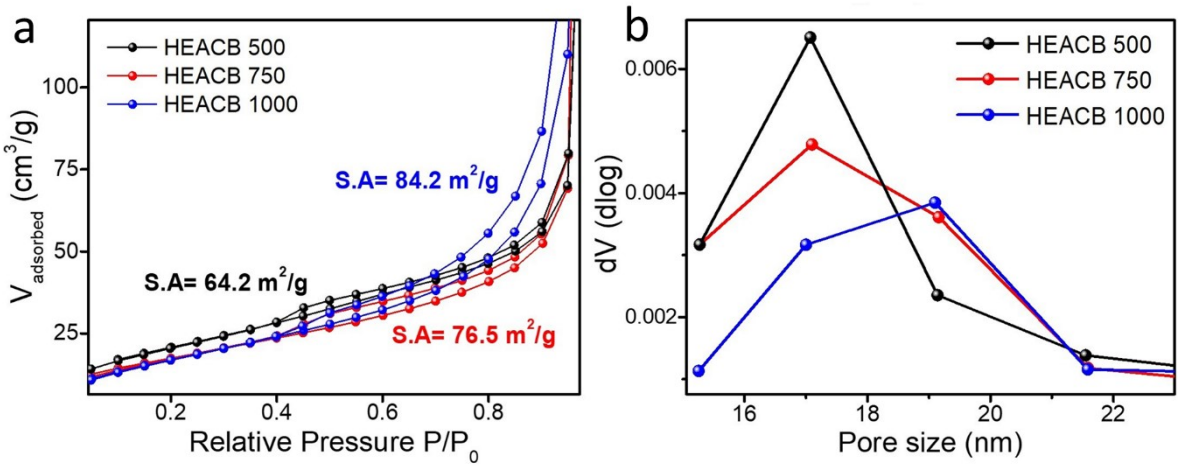

Fig. S13. (a,b) BET surface area measurement of HEACB samples with their pore size distribution plot.

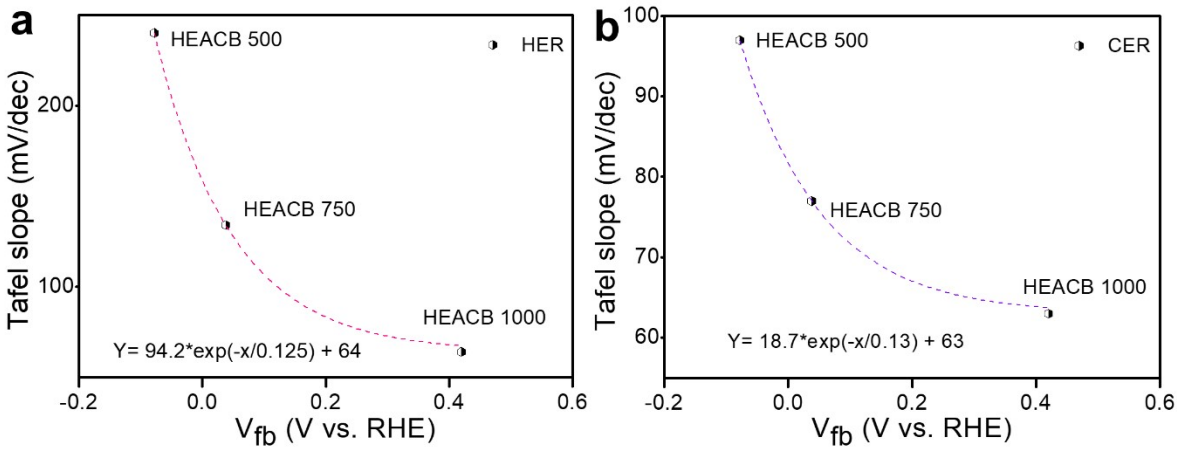

Fig. S14. Tafel slope versus flat band for (a) HER and for (b) CER.

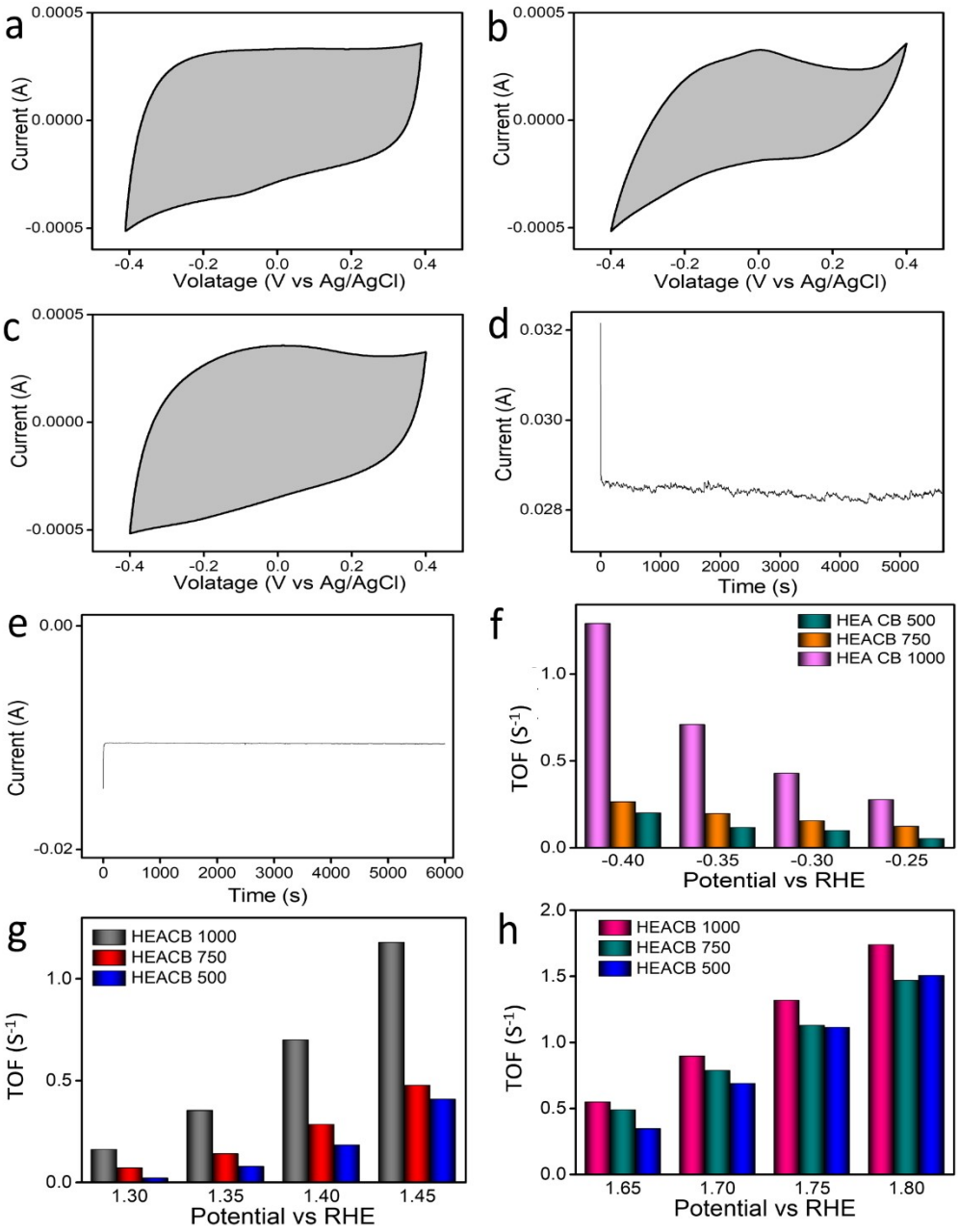

Fig. S15. (a-c) CV curves of HEACB 500, HEACB 750 and HEACB 1000 respectively, (d-e) chrono response of HEACB 1000 under OER and HER polarization region, (f-h) TOF comparison of all the catalysts for HER, CER and OER reactions at different potential.

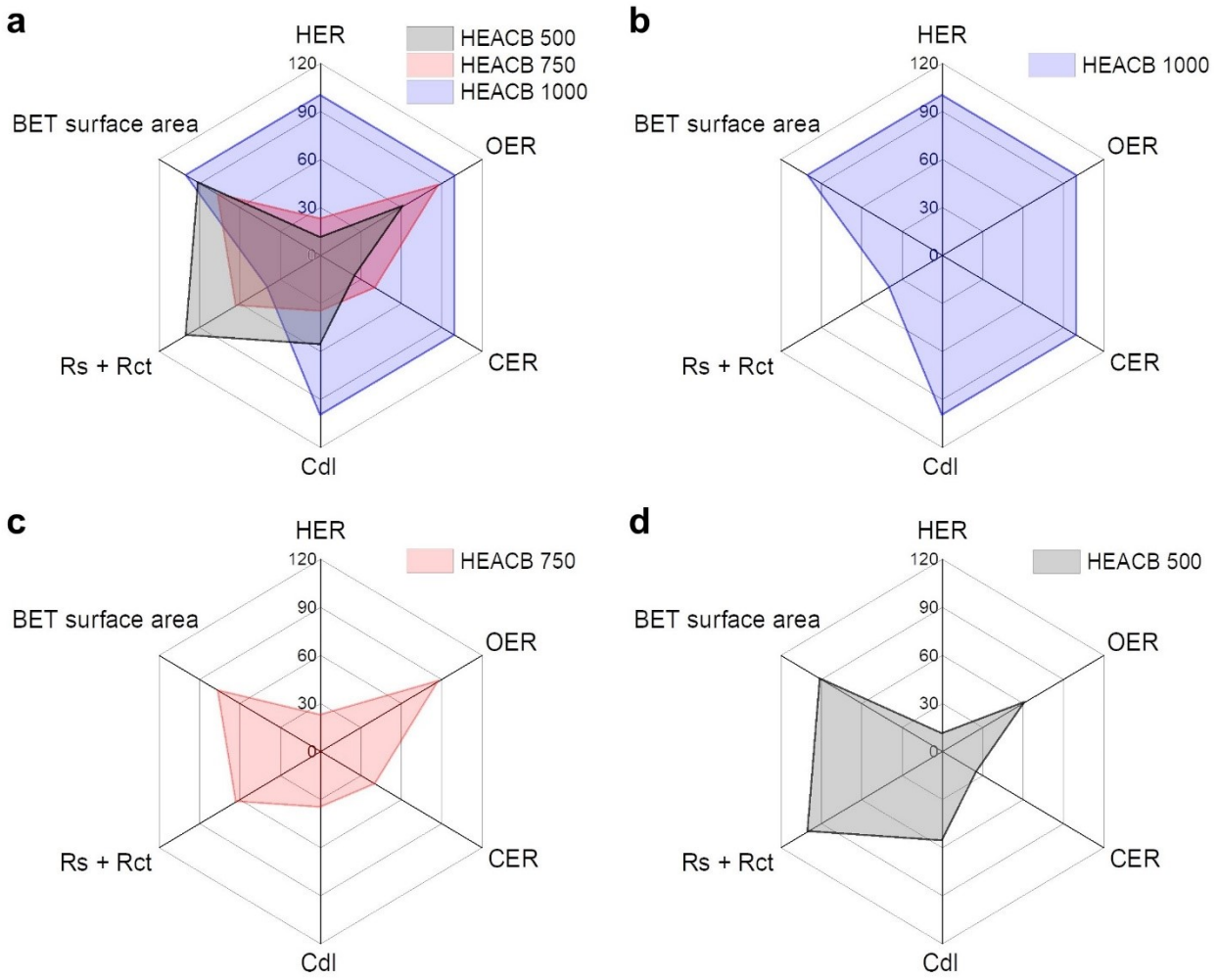

Fig. S16. Relative activity and catalyst characteristic percentages for HEACB samples. (a) Combined plot and (b-d) individual plots.

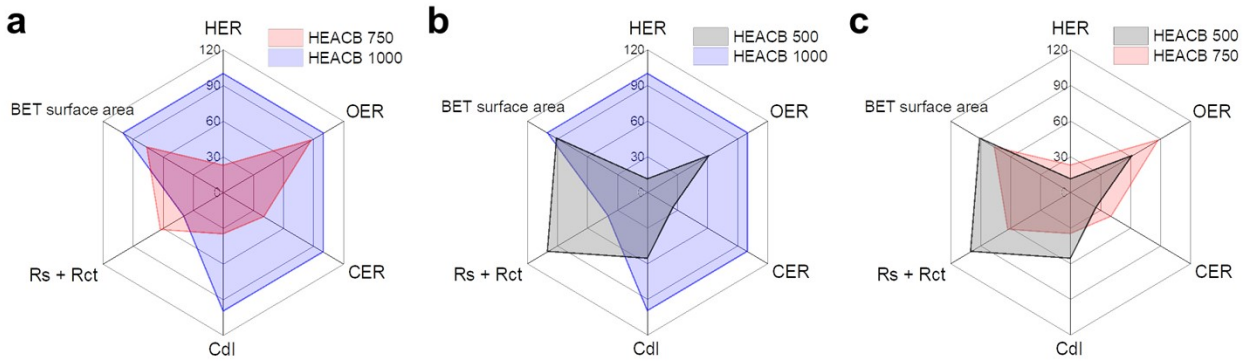

Fig. S17. (a-c) Relative activity and catalyst characteristic percentages for HEACB samples compared to each other in pairs.

Table S1. I_D/I_G and I_{2D}/I_D ratios estimated from the Raman spectra of HEACB 500, HEACB 750, and HEACB 1000.

Annealing temperature (℃)	I_D/I_G	I_{2D}/I_D
500	0.65	0.96
750	0.76	0.31
1000	1.10	0.29

Table S2. Relative atomic percentages of metals in HEACB 1000 deduced from SEM elemental analysis.

Element	**Relative atomic concentration (%)**
Cr	23.7
Mn	32.6
Fe	16.6
Co	13.3
Ni	13.8

Bonds	Position	Relative atomic Concentration (%)
C ─ C/C ═ C	284.78 eV	49.32
C ─ N	285.53 eV	24
C ─ O	287.09 eV	5.32
C ═ O	288.5 eV	8.93
π-π* satellite peak	291.19 eV	12.43

Table S3. Binding energy and atomic percentage of carbon deduced from XPS study.

Table S4. Locations of typical oxygen and their corresponding binding energies deduced from XPS study.

Oxygen location	HEA 500	HEA 750	HEA 1000
Oxygen in lattice ($\mathbf{O_L}$)	530.08 eV	530.49 eV	530.6 eV
Oxygen in vacancy ($\mathbf{O_V}$)	531.52 eV	531.57 eV	531.54 eV
Oxygen at outer surface ($\mathbf{O_S}$)	532.35 eV	532.44 eV	532.42 eV
Adsorbed oxygen ($\mathbf{O_{ads}}$)	533.02 eV	533.04 eV	533.33 eV

Table S5. Binding energy and atomic percentage of oxygen in three samples deduced from XPS studies.

HEACB 500		
Name	**B.E (eV)**	**Relative atomic concentration (%)**
O_V	531.52	17.29
O_L	530.08	4.36
O_S	532.35	53.36
O_{ads}	533.02	24.99

HEACB 750		
Name	**B.E (eV)**	**Relative atomic concentration (%)**
O_V	531.57	20.31
O_L	530.49	7.22
O_S	532.44	52.16
O_{ads}	533.04	20.31

HEACB 1000		
Name	**B.E (eV)**	**Relative atomic concentration (%)**
O_V	531.54	14.02
O_L	530.06	4.23
O_S	532.42	64.14
O_{ads}	533.33	17.61

Table S6. Calculation of TOF for HER for HEACB 1000

Potential vs RHE	S	N	J (mA)	TOF
-0.25	2.97×10^{-4}	3.6×10^{-8}	22.75	0.274
-0.30	2.97×10^{-4}	3.6×10^{-8}	35.31	0.426
-0.35	2.97×10^{-4}	3.6×10^{-8}	58.74	0.708
-0.40	2.97×10^{-4}	3.6×10^{-8}	106.93	1.291

Table S7. Calculation of TOF for HER for HEACB 750

Potential vs RHE	S	N	J (mA)	TOF
-0.25	3.01×10^{-4}	4.8×10^{-8}	10.47	0.121
-0.30	3.01×10^{-4}	4.8×10^{-8}	13.17	0.152
-0.35	3.01×10^{-4}	4.8×10^{-8}	16.81	0.194
-0.40	3.01×10^{-4}	4.8×10^{-8}	22.62	0.262

Table S8. Calculation of TOF for HER for HEACB 500

Potential vs RHE	S	N	J (mA)	TOF
-0.25	1.98×10^{-4}	3.16×10^{-8}	2.88	0.051
-0.30	1.98×10^{-4}	3.16×10^{-8}	5.52	0.097
-0.35	1.98×10^{-4}	3.16×10^{-8}	6.51	0.114
-0.40	1.98×10^{-4}	3.16×10^{-8}	11.25	0.198

Table S9. Elemental ratios of Cr, Mn Fe, Co and Ni in weight and atomic percentages extracted using TEM EDS analysis for HEACB1000 post study.

Elements	Relative weight (%)	Relative atomic concentration (%)
Cr K	22.13	23.34
Mn K	22.87	22.83
Fe K	51.54	50.61
Co K	1.74	1.62
Ni K	1.72	1.60

Table S10. Comparison of activity to other OER, HER, and CER electrocatalysts reported in literature.

Catalyst	Reaction	Electrolyte	Potential at 10 mA cm^{-2} (mV)	Tafel slope (mV dec^{-1})	Ref
A-HEA	OER	1M KOH	277	85	[4]
$FeNi_3$@GCDs-10	OER	1M KOH	238	48.7	[5]
SSNC1	OER	0.1M KOH	-	70	[6]
Ni_6Co_{94} NWs	OER	1M KOH	271	88	[7]
CFGNZ	OER	1M KOH	370	71	[8]
$Fe_1Co_1Ni_1$@N-CNTs-600	OER	1M KOH	249	43.47	[9]
Ni-Fe-Mn	OER	1M KOH	230	79	[10]
NiCoP	OER	1M KOH	295	45	[11]
$(MnFeCoNiCu)S_2$	OER	1M KOH	221	54	[12]
CNF/CoS2-CNT	OER	1M KOH	303	75	[13]
FeZrRu	OER	1M KOH	250	60	[14]
$FeCo_2Mo_5$ LDH	OER	1M KOH	128	72.5	[15]
Mn-NiCo HNS/CNT	OER	1M KOH	239	92	[16]
$MoNi_4$-MX_{10}	OER	1M KOH	122	56	[17]
MoN-Co_2N	OER	1M KOH	267	35.6	[18]
$Ca_{2-x}Sr_xScRuO_6$	OER	1M KOH	323	61	[19]
CoCrFeMnNiP	OER	1M KOH	320	60.8	[20]
$(La_{0.8}Sr_{0.2})_{1+x}MnO_3$	OER	0.1M KOH	-	109	[21]
CoFeNiMnMoPi	OER	1M KOH	270	74	[20]
$SrFe_{0.9}Si_{0.1}O_{3-\delta}$	OER	0.1M KOH	-	58	[6]

$Sr_2Fe_2O_6$@d	OER	0.1M KOH	600	60	[22]
$La_{0.8}Sr_{0.2}MnO_3$	OER	0.1M KOH	256	42.8	[23]
Co/NCNT-25	HER	1M KOH	20	28	[24]
Ni_6Co_{94} NWs	HER	1M KOH	231	105	[7]
Ni-Fe-Mn	HER	1M KOH	64	68	[10]
CuAlNiMoFe	HER	1M KOH	9.7	60	[25]
$Mo_{0.5}Nb_{0.5}Se_2$	HER	0.5 M H_2SO_4	140	46	[26]
Ni/np-Ir	HER	0.5 M H_2SO_4	17.1	24	[27]
CN/CNL/MoS_2/CP	HER	0.5 M H_2SO_4	112	77	[28]
NiIrRuAl-3/1	HER	0.1 M HClO4	14	23	[29]
TiZrNbVTa(Hf) HEAs	HER	1M KOH	-	67	[20]
$Al_{82}Ni_6Co_3Mn_3Y_3Au_3$	HER	0.5 M H_2SO_4	24	43	[30]
Co@Zn-N-NCNT	HER	0.5 M H_2SO_4	67	52.1	[31]
MoS_2@Gr	HER	0.5 M H_2SO_4	120	72	[32]
$(MoWReMnCr)S_2$	HER	0.5M H_2SO_4	229	111	[33]
CoCrFeMnNiP	HER	1M KOH	136	85.5	[34]
PdPtCuNiP	HER	0.5 M H_2SO_4	35.4	34.2	[35]
Rh@PPy	HER	0.5 M H_2SO_4	16	32.5	[36]
MoSSe@f-CNT//VSe_2/rGO/CNT	HER	0.5 M H_2SO_4	249	63	[37]
NiCoFeMnCrP NPs	HER	1M KOH	220	94.5	[33]
Co_1-S_4/NC	HER	0.5 M H_2SO_4	114	60	[38]
$Co(VMnNiZn)PS_3$	HER	1M KOH	66	65.5	[39]
Co_1-S_4/NC	HER	0.5 M H_2SO_4	120	91	[40]
Ni_2P–Co_2P	HER	0.5 M H_2SO_4	94	53.1	[41]

La_2CoMnO_6	CER	5.0 M NaCl	280 @100 mA cm^{-2}	44	[42]
$Ti/Ir_{0.8}Nd_{0.2}O_x$	CER	5.0 M NaCl	160 @100 mA cm^{-2}	45	[43]
Se_NiFe_LDH	CER	5.0 M NaCl	1.54 V @50 mA cm^{-2}	37.4	[44]
RuO_2/IrO_2	CER	5.0 M NaCl	1.115 V vs SCE	33.5	[45]
$CoSb_2O_x$	CER	4.0 M NaCl	444	-	[46]
Ir-2	CER	0.5 M NaCl	258	26	[47]
IrO_2/TiO_2	CER	Sat. NaCl	44	40	[48]
RuO_2 NPs/CC	CER	5.0 M NaCl	1.05 V vs SCE	38	[49]
$RuO_2@TiO_2$-5	CER	Sat. NaCl	80 @50 mA cm^{-2}	39	[50]
Ru_1-TiO_x/Ti	CER	4 M NaCl	46	35	[51]
Pt_1/CNT	CER	1 M NaCl	50	38	[52]
RuO_2/IrO_2-TiO_2 NTAs	CER	5.0 M NaCl	1.115 V (vs. SCE) 50 mA cm^{-2}	33.5	[45]
$Ti/Ir_{0.8}Nd_{0.2}O_x$	CER	5.0 M NaCl	1.52 V at 100 mA cm^{-2}	45.9	[43]
Co_3O_4 nanobelt	CER	5.0 M NaCl	200	66	[53]
IrO_2-Ta_2O_5-TiO_2	CER	4.0 M NaCl	70	40	[54]
HEACB 1000	OER	1 M KOH	350	95	**This work**
HEACB 1000	HER	0.5 M H_2SO_4	190	64	**This work**
HEACB 1000	CER	4 M NaCl and 1 M HCl	30	63	**This work**
HEACB 1000	CER	4 M NaCl and 1 M HCl	79 @ 50 mA/cm^{-2} 163 @ 100 mA/cm^{-2}	63	**This work**

Table S11. Calculation of TOF for OER for HEACB 1000

Potential vs RHE	S	N	J (mA)	TOF
1.65	2.97×10^{-4}	3.6×10^{-8}	45.18	0.545
1.70	2.97×10^{-4}	3.6×10^{-8}	74.13	0.893
1.75	2.97×10^{-4}	3.6×10^{-8}	109.11	1.315
1.80	2.97×10^{-4}	3.6×10^{-8}	144.25	1.737

Table S12. Calculation of TOF for OER for HEACB 750

Potential vs RHE	S	N	J (mA)	TOF
1.65	3.01×10^{-4}	4.8×10^{-8}	41.75	0.484
1.70	3.01×10^{-4}	4.8×10^{-8}	67.63	0.783
1.75	3.01×10^{-4}	4.8×10^{-8}	97.16	1.126
1.80	3.01×10^{-4}	4.8×10^{-8}	126.21	1.146

Table S13. Calculation of TOF for OER for HEACB 500

Potential vs RHE	S	N	J (mA)	TOF
1.65	1.98×10^{-4}	3.16×10^{-8}	19.38	0.342
1.70	1.98×10^{-4}	3.16×10^{-8}	38.82	0.685
1.75	1.98×10^{-4}	3.16×10^{-8}	62.83	1.113
1.80	1.98×10^{-4}	3.16×10^{-8}	85.16	1.504

Table S14. Calculation of TOF for CER for HEACB 1000

Potential vs RHE	S	N	J (mA)	TOF
1.30	2.97×10^{-4}	3.6×10^{-8}	13.52	0.159
1.35	2.97×10^{-4}	3.6×10^{-8}	29.84	0.351
1.40	2.97×10^{-4}	3.6×10^{-8}	59.25	0.698
1.45	2.97×10^{-4}	3.6×10^{-8}	100.06	1.178

Table S15. Calculation of TOF for CER for HEACB 750

Potential vs RHE	S	N	J (mA)	TOF
1.30	3.01×10^{-4}	4.8×10^{-8}	5.92	0.068
1.35	3.01×10^{-4}	4.8×10^{-8}	11.91	0.138
1.40	3.01×10^{-4}	4.8×10^{-8}	24.43	0.282
1.45	3.01×10^{-4}	4.8×10^{-8}	41.07	0.475

Table S16. Calculation of TOF for CER for HEACB 500

Potential vs RHE	S	N	J (mA)	TOF
1.30	3.01×10^{-4}	4.8×10^{-8}	1.022	0.018
1.35	3.01×10^{-4}	4.8×10^{-8}	4.29	0.075
1.40	3.01×10^{-4}	4.8×10^{-8}	10.28	0.181
1.45	3.01×10^{-4}	4.8×10^{-8}	23.22	0.406

References

1 D. B. Miracle and O. N. Senkov, *Acta Mater.*, 2017, **122**, 448–511.

2 T. ul Haq, S. A. Mansour, A. Munir and Y. Haik, *Adv. Funct. Mater.*, 2020, **30**, 1910309.

3 J. Tong, Y. Li, L. Bo, W. Li, T. Li, Q. Zhang, D. Kong, H. Wang and C. Li, *ACS Sustain. Chem. Eng.*, 2019, **7**, 17432–17442.

4 H. Wang, R. Wei, X. Li, X. Ma, X. Hao and G. Guan, *J. Mater. Sci. Technol.*, 2021, **68**, 191–198.

5 Z. Li, X. Xu, X. Lu, C. He, J. Huang, W. Sun and L. Tian, *J. Colloid Interface Sci.*, 2022, **615**, 273–281.

6 X. Xu, Y. Chen, W. Zhou, Y. Zhong, D. Guan and Z. Shao, *Adv. Mater. Interfaces*, 2018, **5**, 1701693.

7 F. Ganci, V. Cusumano, P. Livreri, G. Aiello, C. Sunseri and R. Inguanta, *Int. J. Hydrogen Energy*, 2021, **46**, 10082–10092.

8 L. Sharma, N. K. Katiyar, A. Parui, R. Das, R. Kumar, C. S. Tiwary, A. K. Singh, A. Halder and K. Biswas, *Nano Res.*, 2022, **15**, 4799–4806.

9 Z. Li, L. Cai, M. Song, Y. Shen, X. Wang, J. Li, J. Wang, P. Wang and L. Tian, *Electrochim. Acta*, 2020, **339**, 135886.

10 M. A. Ashraf, C. Li, B. T. Pham and D. Zhang, *Int. J. Hydrogen Energy*, 2020, **45**, 24670–24683.

11 S. Battiato, L. Bruno, A. L. Pellegrino, A. Terrasi and S. Mirabella, *Catal. Today*, , DOI:https://doi.org/10.1016/j.cattod.2022.10.011.

12 F. Li, Y. Ma, H. Wu, Q. Zhai, J. Zhao, H. Ji, S. Tang and X. Meng, *J. Phys. Chem. C*, 2022, **126**, 18323–18332.

13 X. Guo, M. Yu, X. Chang, X. Ma and M. Zhang, *ACS Appl. Nano Mater.*, , DOI:10.1021/acsanm.2c03663.

14 Y. Zhang, Z. Wang, S. Guo, Z. Zhang, X. Zeng, P. Dong, M. Li, J. Xiao, C. Zhang, J. Hu and Y. Zhang, *Electrochim. Acta*, 2022, 141502.

15 Y. Huang, J. Peng, Y. Gao, Z. Wang, J. Li and F. Li, *ACS Appl. Energy*

Mater., 2022, **5**, 12937–12944.

16 K. Wu, C. Cao, K. Li, C. Lyu, J. Cheng, H. Li, P. Hu, J. Wu, W.-M. Lau, X. Zhu, P. Qian and J. Zheng, *Chem. Eng. J.*, 2023, **452**, 139527.

17 X. Zhao, K. Tang, C. Lee, C.-F. Du, H. Yu, X. Wang, W. Qi, Q. Ye and Q. Yan, *Small*, 2022, **18**, 2107541.

18 X. Wang, X. Han, R. Du, C. Xing, X. Qi, Z. Liang, P. Guardia, J. Arbiol, A. Cabot and J. Li, *ACS Appl. Mater. Interfaces*, 2022, **14**, 41924–41933.

19 N. Kumar, T. Rom, M. Kumar, T. C. Nagaiah, E. Lee, H. C. Ham, S. H. Choi, S. Rayaprol, V. Siruguri, T. K. Mandal, B. J. Kennedy and A. K. Paul, *ACS Appl. Energy Mater.*, 2022, **5**, 11632–11645.

20 B. Sarac, V. Zadorozhnyy, Y. P. Ivanov, F. Spieckermann, S. Klyamkin, E. Berdonosova, M. Serov, S. Kaloshkin, A. L. Greer, A. S. Sarac and J. Eckert, *Corros. Sci.*, 2021, **193**, 109880.

21 W. Xu, N. Apodaca, H. Wang, L. Yan, G. Chen, M. Zhou, D. Ding, P. Choudhury and H. Luo, *ACS Catal.*, 2019, **9**, 5074–5083.

22 R. K. Hona and F. Ramezanipour, *Angew. Chemie Int. Ed.*, 2019, **58**, 2060–2063.

23 H. Wang, L. Yan, T. Nakotte, W. Xu, M. Zhou, D. Ding and H. Luo, *Inorg. Chem. Front.*, 2019, **6**, 1029–1039.

24 Z. Li, L. Zang, Q. Xu, F. Shen, J. Wang, Y. Zhang, Y. Zhang and L. Sun, *New J. Chem.*, 2022, **46**, 20809–20816.

25 R.-Q. Yao, Y.-T. Zhou, H. Shi, W.-B. Wan, Q.-H. Zhang, L. Gu, Y.-F. Zhu, Z. Wen, X.-Y. Lang and Q. Jiang, *Adv. Funct. Mater.*, 2021, **31**, 2009613.

26 I. S. Kwon, I. H. Kwak, J. Y. Kim, T. T. Debela, Y. C. Park, J. Park and H. S. Kang, *ACS Nano*, 2021, **15**, 5467–5477.

27 Y. Yu, K. Jiang, M. Luo, Y. Zhao, J. Lan, M. Peng, F. M. F. de Groot and Y. Tan, *ACS Nano*, 2021, **15**, 5333–5340.

28 J. Dong, X. Zhang, J. Huang, J. Hu, Z. Chen and Y. Lai, *Chem. Eng. J.*, 2021, **412**, 128556.

29 N. Liu, K. Yin, C. Si, T. Kou, Y. Zhang, W. Ma and Z. Zhang, *J. Mater. Chem. A*, 2020, **8**, 6245–6255.

30 X. Liu, S. Ju, P. Zou, L. Song, W. Xu, J. Huo, J. Yi, G. Wang and J.-Q.

Wang, *J. Alloys Compd.*, 2021, **880**, 160548.

31 Q. Cao, Z. Cheng, J. Dai, T. Sun, G. Li, L. Zhao, J. Yu, W. Zhou and J. Lin, *Small*, 2022, **18**, 2204827.

32 H. T. Bui, D. C. Linh, L. D. Nguyen, H. Chang, S. A. Patil, N. K. Shrestha, K. X. Bui, T. S. Bui, T. N. A. Nguyen, N. T. Tung, S.-H. Han and P. T. San, *J. Mater. Sci.*, 2022, **57**, 18993–19005.

33 D. Lai, Q. Kang, F. Gao and Q. Lu, *J. Mater. Chem. A*, 2021, **9**, 17913–17922.

34 X. Zhao, Z. Xue, W. Chen, Y. Wang and T. Mu, *ChemSusChem*, 2020, **13**, 2038–2042.

35 Y. Li, J. Tang, H. Zhang, Y. Wang, B. Lin, J. Qiao, H. Zheng, Z. Yu, Y. Liu, T. Zhou and X. Lei, *Chem. Eng. J.*, 2023, **453**, 139905.

36 W. Wang, K. Deng, Q. Mao, H. Yu, Z. Wang, Y. Xu, X. Li, L. Wang and H. Wang, *Nanotechnology*, 2023, **34**, 45402.

37 N. Kuniyil, S. R. Koottumvathukkal Anil Raj and C. S. Rout, *Energy & Fuels*, 2022, **36**, 13346–13355.

38 H. Tang, H. Gu, Z. Li, J. Chai, F. Qin, C. Lu, J. Yu, H. Zhai, L. Zhang, X. Li and W. Chen, *ACS Appl. Mater. Interfaces*, 2022, **14**, 46401–46409.

39 R. Wang, J. Huang, X. Zhang, J. Han, Z. Zhang, T. Gao, L. Xu, S. Liu, P. Xu and B. Song, *ACS Nano*, 2022, **16**, 3593–3603.

40 Y. Gao, D. Zhang, J. Li, H. Gong, C. Jiang, H. Xue, X. Huang, T. Wang and J. He, *Chem. – A Eur. J.*, 2022, **n/a**, e202202410.

41 H. Zhong, G. Liu, Y. Cao, B. Chen, M. Ye and J. Shen, *ACS Appl. Energy Mater.*, 2022, **5**, 12059–12066.

42 K. Sood, S. Rana, R. Wadhwa, K. K. Bhasin and M. Jha, *Adv. Mater. Interfaces*, 2022, **9**, 2201138.

43 J. Hu, H. Xu, X. Feng, L. Lei, Y. He and X. Zhang, *ChemElectroChem*, 2021, **8**, 1204–1210.

44 W.-H. Hung, B.-Y. Xue, T.-M. Lin, S.-Y. Lu and I.-Y. Tsao, *Mater. Today Energy*, 2021, **19**, 100575.

45 W. Cheng, Y. Liu, L. Wu, R. Chen, J. Wang, S. Chang, F. Ma, Y. Li and H. Ni, *Catal. Today*, 2022, **400**–**401**, 26–34.

46 I. A. Moreno-Hernandez, B. S. Brunschwig and N. S. Lewis, *Energy Environ. Sci.*, 2019, **12**, 1241–1248.

47 J. S. Ko, J. K. Johnson, P. I. Johnson and Z. Xia, *ChemCatChem*, 2020, **12**, 4526–4532.

48 Y. Wang, Y. Xue and C. Zhang, *Small*, 2021, **17**, 2006587.

49 F. Zhang, X. Gu, S. Zheng, H. Yuan, J. Li and X. Wang, *Electrochim. Acta*, 2019, **307**, 385–392.

50 J. Huang, M. Hou, J. Wang, X. Teng, Y. Niu, M. Xu and Z. Chen, *Electrochim. Acta*, 2020, **339**, 135878.

51 Y. Yao, L. Zhao, J. Dai, J. Wang, C. Fang, G. Zhan, Q. Zheng, W. Hou and L. Zhang, *Angew. Chemie Int. Ed.*, 2022, **61**, e202208215.

52 T. Lim, G. Y. Jung, J. H. Kim, S. O. Park, J. Park, Y.-T. Kim, S. J. Kang, H. Y. Jeong, S. K. Kwak and S. H. Joo, *Nat. Commun.*, 2020, **11**, 412.

53 X. Zhu, P. Wang, Z. Wang, Y. Liu, Z. Zheng, Q. Zhang, X. Zhang, Y. Dai, M.-H. Whangbo and B. Huang, *J. Mater. Chem. A*, 2018, **6**, 12718–12723.

54 L. Deng, Y. Liu, G. Zhao, J. Chen, S. He, Y. Zhu, B. Chai and Z. Ren, *J. Electroanal. Chem.*, 2019, **832**, 459–466.